Effect of Precipitate Embryo Induced by Strain on Natural Aging and Corrosion Behavior of 2024 Al Alloy

Tao Zhang [1,2,3], Hongyun Luo [1,2,3,*], Yuqin Su [1,*], Pingwei Xu [1], Jun Luo [1,2,3] and Sijie Li [1,2,3]

[1] Key Laboratory of Aerospace Materials and Performance (Ministry of Education), School of Materials Science and Engineering, Beihang University, Beijing 100191, China; ztwuai@126.com (T.Z.); xpw2012buaa@gmail.com (P.X.); luojunxt@126.com (J.L.); 18014128516@163.com (S.L.)

[2] The Collaborative Innovation Center for Advanced Aero-Engine (CICAAE), Beihang University, Beijing 100191, China

[3] Beijing Key Laboratory of Advanced Nuclear Materials and Physics, Beihang University, Beijing 100191, China

* Correspondence: lhy@buaa.edu.cn (H.L.); suyuqin@buaa.edu.cn (Y.S.); Tel.: +86-10-8233-9905 (H.L.); Fax: +86-10-8231-7108 (H.L.)

Abstract: Pre-aging precipitates in 2024 Al alloy re-dissolved during rolling, and Mg and Cu atoms were enriched in the dislocation structure to form "precipitate embryo", which is beneficial for the formation of second phase during the subsequent natural aging process. Due to the solubility of the large precipitate particles during deformation, the precipitates in the natural aging 2024 Al alloy were consist of two parts: The undissolved pre-precipitates and the natural aging precipitates derived from the embryos. The electrochemical corrosion behavior and passive film of the samples with different pre-aging time and strain were investigated by electrochemical tests and SEM. The results showed that the corrosion resistance and the passive film performance were deteriorated with the increase of pre-aging time due to the simultaneous increase of the quantity of the two-parts precipitates. The corrosion resistance can be improved by the increase of strain, because there will be smaller grain size and the existence of large undissolved precipitates in smaller strain samples.

Keywords: precipitate embryo; aging treatment; severe plastic deformation; corrosion resistance; passive film

1. Introduction

Age-hardened Al alloy 2024 (AA2024) is a kind of structural material that possesses excellent properties such as high strength, light weight, good toughness and excellent formability. These advantages make it widely used in the aerospace and automotive industries. Precipitates lead to excellent mechanical properties [1–4], but a basic problem is presented due to the increasing pitting susceptibility of precipitate, particularly for the Mg-rich particles [5–9].

The aging sequence of AA 2024 after solid solution treatment (SST) is SST–GPB (Guinier-Preston-Bagaryatsky zones)–S′–S [10,11]. They keep coherent, semi-coherent and non-coherent with the matrix, respectively. All of them are enriched in Mg and Cu, decomposed from the dissolution of supersaturated solid solution with a rate depend on the temperature. The local corrosion sensitivity is greatly influenced by these precipitation particles [5,7,8,12]. Guan et al. [9] investigated the pitting behavior of Al–Mg alloy with nanoscale β phase, revealing that the rate of pitting corrosion depends on the number and size of β particles. With the increase of aging time, the average size of the β phase increases and the pitting potential decreases. In Al–Cu alloys, the GPB zones increases with time, until it reaches the saturation state of precipitated phase, and the addition of Mg accelerates the natural

aging process [13]. Therefore, the pitting susceptibility caused by the precipitation phase is almost inevitable. While precipitates are preferentially nucleated at defects (such as dislocation and grain boundary) enriched in Cu and Mg. Thus intergranular corrosion easily occurs in deformed Al alloys after aging due to the formation of grain boundary precipitates [12] and may result in catastrophic failure of alloy structures. An efficient way to minimize intergranular corrosion is the inhibition the formation of grain boundary precipitates, which is realized by introducing "precipitate embryos" in the grains before re-aging [14–17]. The role of the embryo is to determine that the precipitated phase preferentially nucleates within the grain rather than on the grain boundary.

The crystal structure of the embryo may be the same or close to that of the final particles. In the Al alloys, solute clusters such as the GP and GPB zones meet such condition. These cluster structures are easily formed in severely deformed materials. In this case, certain precipitations can be introduced before deformation, and dissolved into the matrix induced by strain. Subsequently, the re-dissolved solute atoms are segregated to dislocation structure to form embryos. Precipitates are reported to be dissolved by strain in Al–Cu alloy [17–19] and Al–Cu–Mg alloy [15]. However, the number and size of precipitates significantly limit the dissolution, i.e., it is difficult for large particles to re-dissolve.

Our previous work found that, after re-aging, the sample with optimized embryo structure can obtain higher density and finer size precipitates, which not only have strong pinning effect on dislocation motion, but also bear certain deformation. Therefore, it makes an important contribution to both strength and tensile plasticity [1]. To better use the nuclear embryo strengthening and toughening process to guide the design of structural materials, it is necessary to further explore its effect on corrosion resistance which were rarely reported so far. Our previous works investigated the possible mechanism and corresponding mechanical properties [1,2,20,21], and also revealed the corrosion and passivation behavior in deformed Al alloy [22–24]. The goal of this paper is to prepare "precipitate embryo" by pre-aging plus cold deformation (rolling) followed by re-aging, and then study the corrosion and passive film properties of the re-aging samples. The mechanism of corrosion and passivation were discussed by means of open circuit potential (OCP), potentiodynamic polarization (PDP), electrochemical impedance spectroscopy (EIS) and Mott–Schottky (M–S) analyses. Besides, the microstructural changes were characterized by optical micrograph (OM), X-ray diffraction (XRD), scanning transmission electron microscopy (STEM) and scanning electron microscopy (SEM).

2. Materials and Experimental Procedure

2.1. Material Preparation

The chemical composition of the sample AA 2024 used in this paper is shown in Table 1. The as-received AA 2024 may be segregated or contain insoluble precipitate phase. Therefore, the samples were subjected to solid solution treatment (SST) at 768 K for 10 h and then immediately water quenched. After solution treatment, samples were subjected to aging (pre-aging) at 433 K for various times to obtain precipitation phases with different characteristics. All the samples were then subjected to the rolling process with strain rate of $<1\ s^{-1}$. It is worth noting that each roll pass is reduced by only $<5\%$ to avoid splitting. After deformation, all the samples are subjected to re-aging treatment. To avoid recrystallization or dislocation reversion but mainly focus on precipitation phase, the re-aging was conducted at room temperature (natural aging, NA). The whole process is shown in Table 2.

Table 1. Chemical composites of the AA 2024 (wt %).

Element	Cu	Mg	Mn	Fe	Si	Zn	Cr	Ti	Al
AA 2024	4.30	1.50	0.60	0.50	0.50	0.30	0.10	0.02	Bal.

Table 2. Processing of the studied AA 2024. The sample ID means: Pre-aging time–strain–NA.

Sample ID	Solid Solution Treatment (SST, 768 K)	Artificial Aging (433 K)	Rolling Strain	Natural Aging (NA)
10-27-NA	10 h	10 h	27%	365 day
10-40-NA	10 h	10 h	40%	365 day
10-50-NA	10 h	10 h	50%	365 day
10-80-NA	10 h	10 h	80%	365 day
SST-80-NA	10 h	–	80%	365 day
23-80-NA	10 h	23 h	80%	365 day
43-80-NA	10 h	43 h	80%	365 day
93-80-NA	10 h	93 h	80%	365 day

2.2. Microstructural Characterization

Specific microstructures and precipitate characteristics were characterized using scanning transmission electron microscopy (STEM, Tecnai G^2 F20, FEI, Hillsboro, OR, USA) with EDS (X-ray energy dispersive spectrometer, Tecnai G^2 F20, FEI, Hillsboro, OR, USA) detector. After mechanically grinding, disk samples with diameter of 3 mm for STEM analysis were prepared using a Gatan Dual Ion Milling System (Type 691, Gatan, Pleasanton, CA, USA) with an Ar^+, followed by plasma cleaning. Besides, the phase composition analysis was completed by XRD (Rigaku D/max2500PC, Rigaku, Tokyo, Japan) with an exactly the same method used in our previous work [1].

2.3. Electrochemical Test

The working electrode is adhered to copper wire by conductive copper powder, and the test part is sealed with epoxy resin in the PVC pipe leaving an active area of 7 mm × 7 mm. Before electrochemical testing, the working electrode was polished to 5000# by sandpaper, then cleaned by acetone to remove oil then rinsed with distilled water. Electrochemical tests were performed using the CHI660b electrochemical workstation (Chenhua Co., Shanghai, China). The electrochemical measurements were conducted using a three-electrode cell comprising a thin platinum plate as the counter electrode, a saturated calomel electrode (SCE) as the reference electrode and the sample as the working electrode. All the potential values mentioned in this work are measured with respect to the value of SCE.

The solution applied to evaluate the corrosion process was 0.1 M NaCl solution. In addition, to test the features of passive films on Al alloys with different treatments, borate buffer solution (0.5 M H_3BO_3 and 0.05 M $Na_2B_4O_7 \cdot 10H_2O$; pH 7.8) were also used. To ensure the reliability and repeatability of the experiment, at least 4 replicate samples were used for each experiment. To avoid the influence of previous experiments on subsequent experiments, for example, the surface of the sample tested by polarization curve has been corroded seriously, and cannot continue to do EIS or M–S experiments. Therefore, all experiments are carried out on individual samples. All 2024 Al alloy samples were immersed at OCP condition in the test solution to reach the steady-state before any electrochemical tests (2400 s in NaCl solution, 3600 s in borate buffer solution). All electrochemical tests were performed as follows:

(a)　EIS analysis was carried out starting from 10^5 Hz to 0.01 Hz at OCP condition with an AC voltage amplitude of 50 mV.

(b)　PDP plots were measured starting from −0.3 V (vs. OCP) to +0.5 V (vs. OCP) in 0.1 M NaCl solution, and from OCP to +2 V (vs. OCP) in borate buffer solution. The scan rate was 1 mV/s.

(c)　M–S curves (borate buffer solution) were measured starting from −2 V (vs. SCE) to +0.5 V (vs. SCE) (step potential = 50 mV and frequency = 1 kHz).

2.4. Morphology Observation

To examine the surface topography of the AA 2024, an optical microscope of the type Leica DM 4000 (Leica, Wetzlar, Germany) was used. The samples were polished and etched with Keller's reagent (1 mL HF + 1.5 mL HCl + 2.5 mL HNO$_3$ + 95 mL H$_2$O) [13]. The corrosion morphology of Al alloy in sodium chloride solution and the morphology of passivation film formed in borate buffer solution were observed in scanning electron microscopy (SEM, VEGA3 TESCAN, Tescan, Brno Czech; acceleration voltage 20 kV). Some samples were immersed in the same solution as the electrochemical test for 4 h or 24 h, then dried in cold air flow.
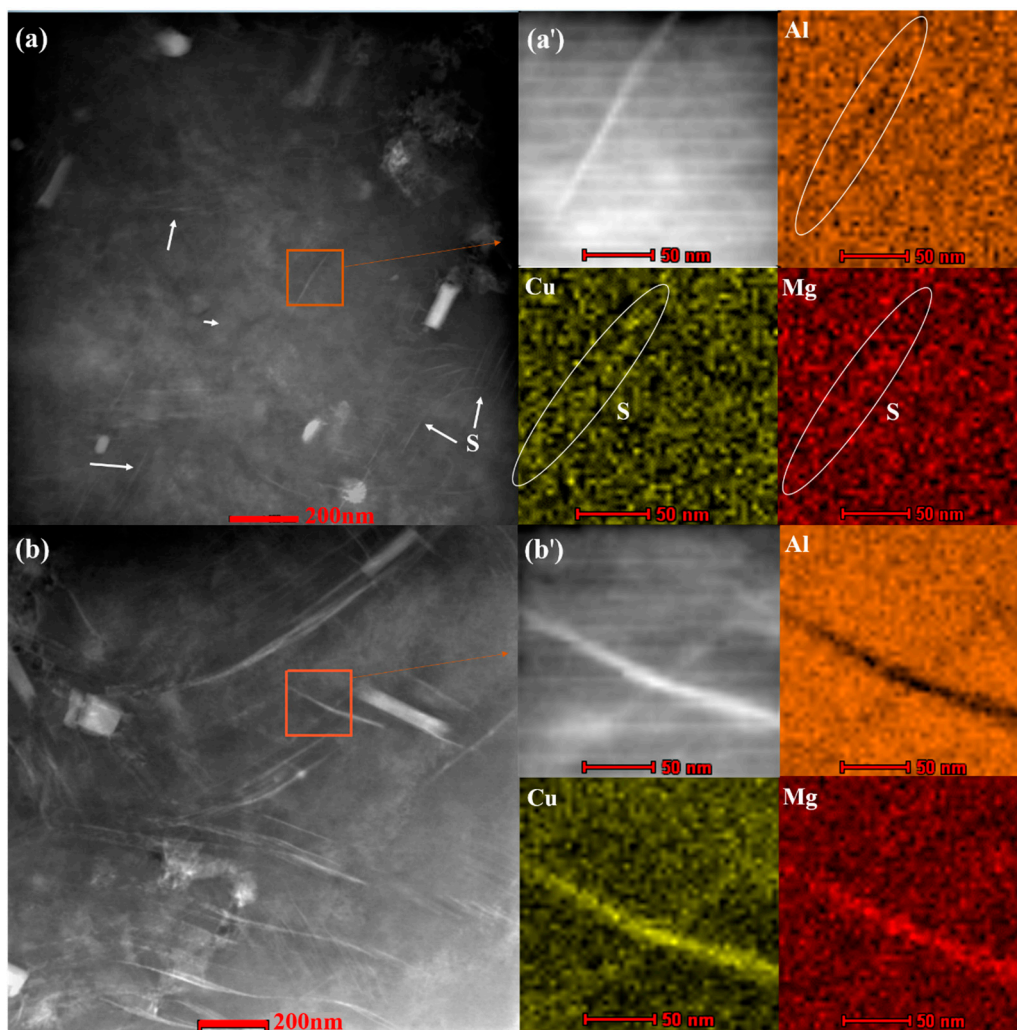
3. Results

3.1. Microstructure

The microstructures obtained by STEM from samples 10-50-NA, 10-80-NA, SST-80-NA, 23-80-NA, 43-80-NA and 93-80-NA are shown in Figures 1–3.
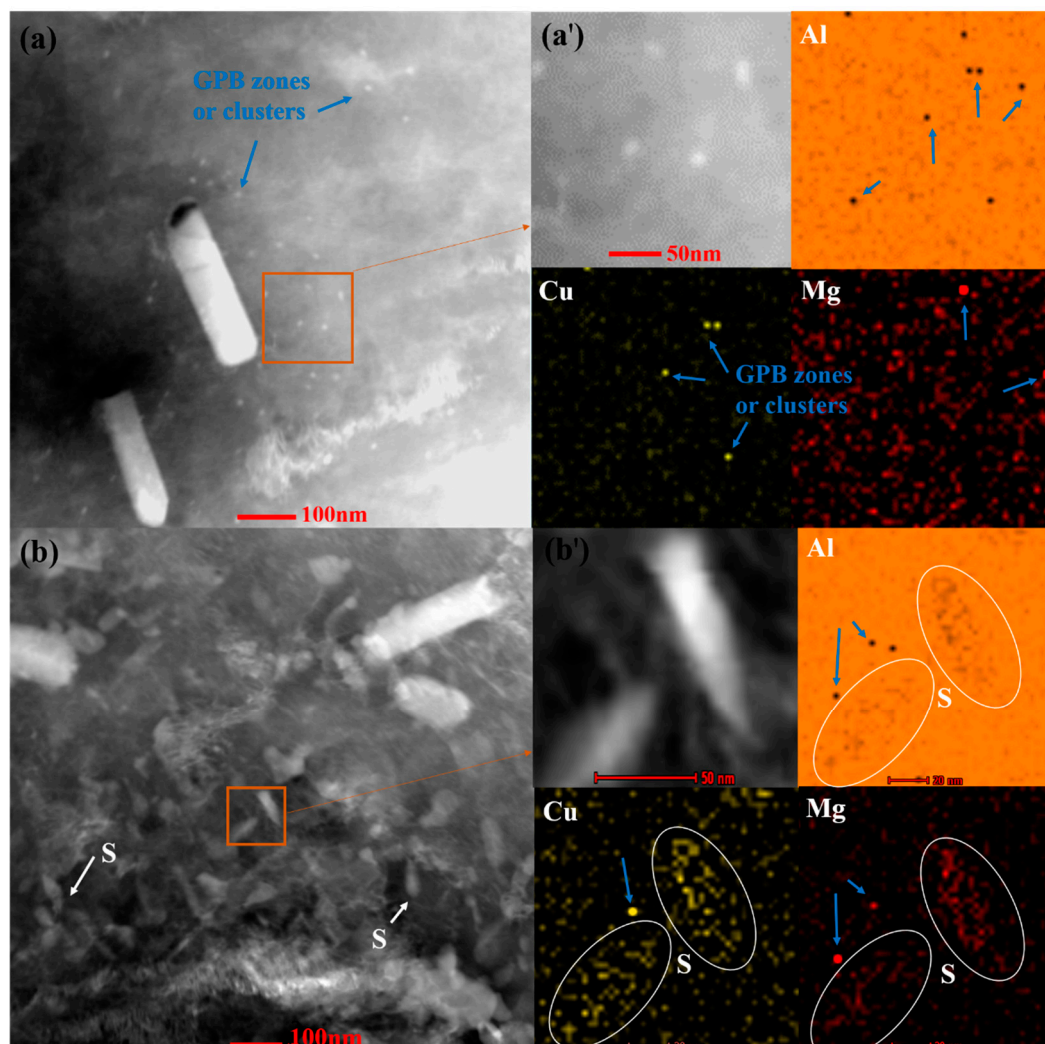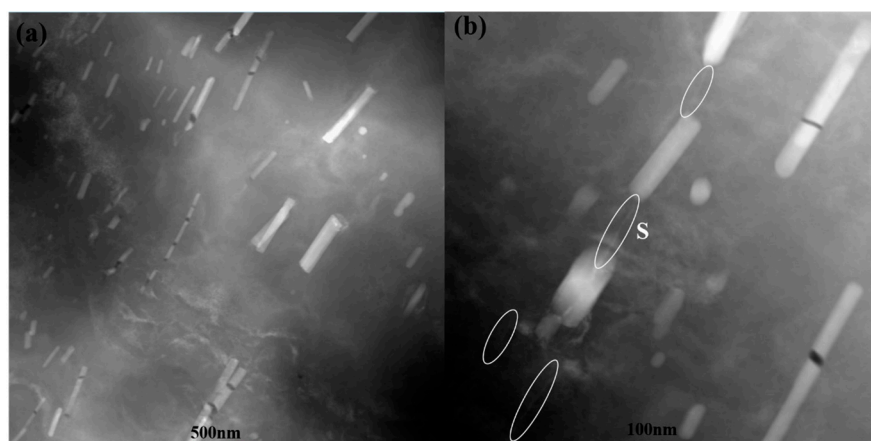

Figure 1. STEM-HAADF images and elemental maps for: (**a**,**a′**): SST-80-NA; (**b**,**b′**) 23-80-NA. GPB zones or clusters enriched with Cu or Mg were observed marked with blue arrows. S phase were surrounded by while circles.
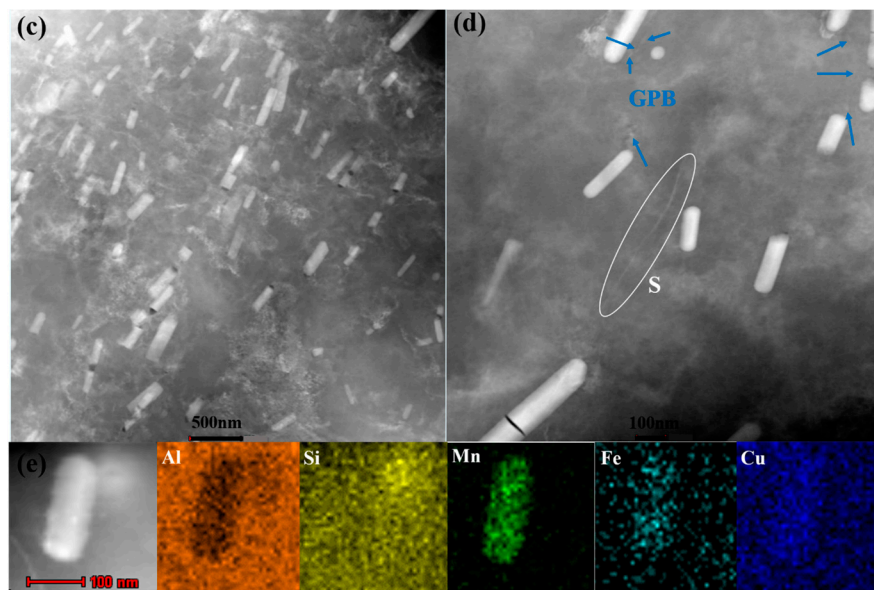
Figure 2. STEM-HAADF images and elemental maps for: (**a**,**a′**) 43-80-NA; (**b**,**b′**) 93-80-NA. The white arrows and circles represent the S phase.


Figure 3. *Cont.*

Figure 3. STEM-HAADF images and elemental maps for: (**a**,**b**): 10-50-NA and (**c**,**d**) 10-80-NA. GPB zones or clusters were marked with blue arrows. S phase were surrounded by while circles; (**e**) Elemental map of T phase riching in Si, Mn, Fe and Cu.

For sample SST-80-NA, the microstructural feature is very evident: some sporadic scattered Cu and Mg "atomic clusters" or GPB zones with relatively small volume fraction (Figure 1a). The darker points detected on the elemental map tend to enrich only one element of Cu or Mg (Figure 1a′), indicating that they are still in the early stage of nucleation. After aging for 23 h, a large number of nano-sized S precipitates and some clusters or GPB zones appear, as shown in Figure 1b. The amount of S precipitate is slightly increased in 43-80-NA, compared with the corresponding case of 23 h aging (Figure 2a). An extensive network of large S-phase laths is present at 93 h of aging (Figure 2b), and the length of the S phase reached hundreds of nanometers in 93-80-NA (Figure 2b), which is approximately several times of the laths present after 23 or 43 h of aging. High density of dislocations are tangled inside all the deformed samples, which are beneficial for the formation of precipitate embryos. As the strain increases, the dislocation density increases significantly (Figure 3a,c). S phase particles were observed in 10-50-NA (Figure 3b), while some GPB zones were detected in 10-80-NA (Figure 3d). Rod-shaped T-phase dispersoids are randomly distributed in the matrix and the elemental maps show that the T phase is enriched in Fe, Mg, Si and Cu (Figure 3e). The variation in size and number of particles could be of significant importance in terms of pitting susceptibility, and will be discussed later.

Figure 4a–c depicts the optical microscopy micrograph of the natural aging AA 2024. The surfaces of the samples are very smooth overall with relatively low roughness. As the pre-aging time was extended, black spots increased slightly. Larger black spots may be inclusions or intermetallic compounds (such as undissolved θ (Al_2Cu) or Fe-rich phases [13])), and small ones maybe the pits caused by the corrosion of the keller reagent (Figure 4a–c). The XRD patterns of different pre-aging time samples are very similar (Figure 4d) with (220) preferred orientation, and they are basically remain unchanged after rolling [1]. The crystallite (sub-grain) sizes calculated from the XRD result [3,13] of samples with 80% strain is about 200 nm, almost the same as the rolling state [1]. While the he sub-grain size of the 40% strain and 27% strain samples reached about 800 nm~1 μm. The grain boundary of the original equiaxed grain is damaged in the rolling process to form sub-grain, and it is slow to recover at room temperature.
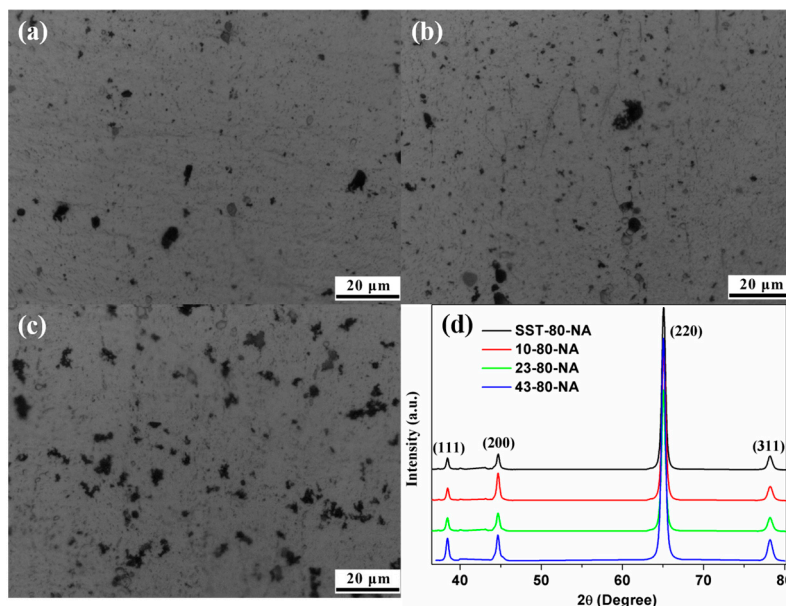
Figure 4. Surface topography of natural aging samples: (**a**) SST-80-NA; (**b**) 10-80-NA; (**c**) 93-80-NA; and (**d**) their corresponding XRD patterns.

3.2. Corrosion Behavior Measurements

Representative plots of the OCP of samples with different strain in 0.1 M NaCl solution are shown in Figure 5a. The reproducibility of experimental curves for per case of study is very good, and for the convenience of observation, one of them is used for display (the same applies hereinafter). It took about 350 s before 10-27-NA and 10-40-NA to reach a relatively steady-state, although the transient currents of 10-27-NA still remain very large in the later stage, which is indicative of pitting event. The OCP shifts to noble values with the increasing of strain. The sample with 80% thickness reduction possesses the highest OCP and spends a minimum time to reach stable state, indicating the minimum corrosion tendency. The results show that the corrosion resistance is improved with strain increasing, and the PDP plots and EIS tests were carried out to further investigate the electrochemical characteristics of all the samples.

The PDP curves in 0.1 M NaCl solution are presented in Figure 5b. The pitting formation potential (E_{pit}) is very close to and even lower than the corrosion potential (E_{corr}). Therefore, no obvious passivation behavior was observed, which is consistent with the results in other's work [25]. The anodic dissolution zone is wide, and the anodic current increases fast. The cathodic branch can be divided into three stages [26]. Stage I is the weak polarization region just below the OCP. Stage II with high cathodic overpotential represents the diffusion controlling region of oxygen reduction zone. Oxygen reduction reaction mainly occurred in the stage I and II:

$$O_2 + 2H_2O + 4e \rightarrow 4OH^- \tag{1}$$

Thus, $Al(OH)_3$ can be formed on the electrode:

$$Al^{3+} + 3OH^- \rightarrow Al(OH)_3\downarrow \tag{2}$$

which could prevent oxygen reduction on the electrode surface as a kind of colloidal precipitate. Therefore, the current density rise slowly in stage II. The current density increases rapidly in stage III due to the hydrogen evolution reaction. The E_{corr} and corrosion current (I_{corr}) were obtained by Tafel extrapolation method as shown in Table 3 (The fitting error analysis of duplicate samples were also annotated). The E_{corr} of these four samples is between −0.53 V and −0.56 V. Compared with

the 80% strain alloy (about 1.38 μA/cm^2), the I_{corr} of 10-27-NA increased by 0.2 μA/cm^2, reaching 1.58 μA/cm^2. The cathodic current density of 10-27-NA fluctuates greatly in stage II, indicating that the chemical stability is slightly worse and there are many transient processes.
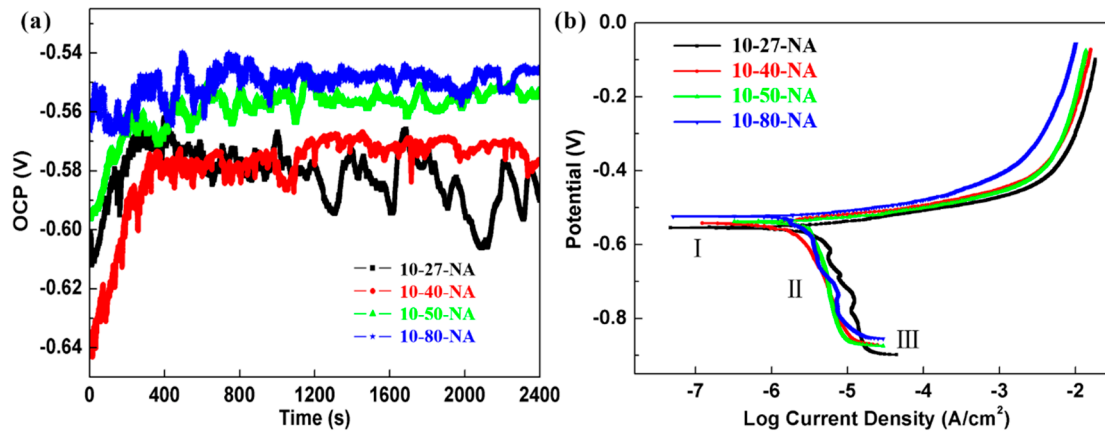

Figure 5. (**a**) The OCP and (**b**) PDP plots with scan rate of 1 mV/s of the AA 2024 with different strain in 0.1 M NaCl solution.

Table 3. The parameters of the PDP plots of samples with different strain in 0.1 M NaCl solution.

Sample ID	E_{corr} (V)	I_{corr} (μA/cm^2)
10-27-NA	-0.56 ± 0.02	1.58 ± 0.04
10-40-NA	-0.54 ± 0.01	1.45 ± 0.02
10-50-NA	-0.54 ± 0.01	1.44 ± 0.02
10-80-NA	-0.53 ± 0.01	1.38 ± 0.04

Figure 6 shows the EIS curves obtained in 0.1 M NaCl solution of samples with different strain. All Nyquist graphs share the same shape with two apparent depressed capacitive arcs, indicating that at least two different reaction processes are involved. The high frequency arcs of 10-80-NA and 10-50-NA samples is slightly larger (Figure 5a). Two time constants are observed in the Bode plot, which is consistent with the Nyquist plot, indicating that the AA 2024 is sensitive to Cl$^-$ and is susceptible to pitting corrosion [7,27].
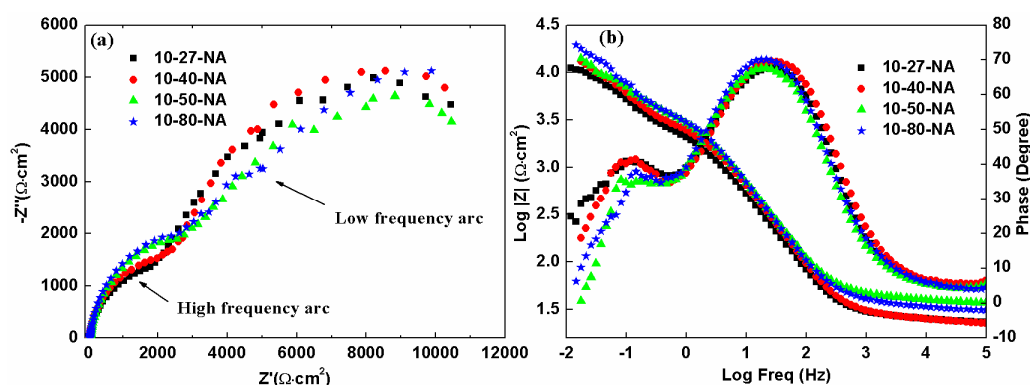
Figure 6. (**a**) Nyquist and (**b**) Bode plots of AA 2024 with different strain in 0.1 M NaCl solution.

To simulate the EIS data, the equivalent circuit with two time constants in Figure 7a is applied. The equivalent circuit consists of the solution resistance (R_s), charge transfer resistance (R_{ct}) and double layer capacitance (Q_{dl}). R_l and Q_l are related to the impedance and capacitance of the oxide layer

formed in the air of the AA 2024. In this system, pitting corrosion of the oxide film leads to the time constant at low frequency and is affected by precipitated particles. Q is the constant phase element to compensate the surface heterogeneity and inhomogeneity. The capacitance of Q can be calculated by the Equation [28]:

$$C_f = Y_0 \cdot (\omega_{max})^{n-1} \tag{3}$$

where Y_0 and n are the fitting parameters of Q that are obtained by fitting EIS data with ZsimpWin software (version 3.10) and ω_{max} is the angular frequency at which the imaginary part of the impedance (Z'') has the maximum value. The value of the capacitance is proportional to the Y_0 according to Equation (3). Fitting of the equivalent circuit was performed by means of professional computer program ZsimpWin and this equivalent circuit has been successfully used in our work and an example (sample 10-40-NA) of the fitted EIS plots are given in Figure 7b,c. The value of fitting parameters are shown in Table 4. The Y_{dl} of the double layer capacitance decreased with the increasing of strain. The R_{ct} of the four samples was 5150, 6209, 6750 and 8939 $\Omega \cdot cm^2$, respectively, and increased with strain, which is the result of the combined effect of grain size and precipitates and will be discussed in Section 4. Due to the continuous filling-overflow-re-filling process of corrosion products in the corrosion pits, Y_1 and R_1, which represent corrosion reactions, changed irregularly.
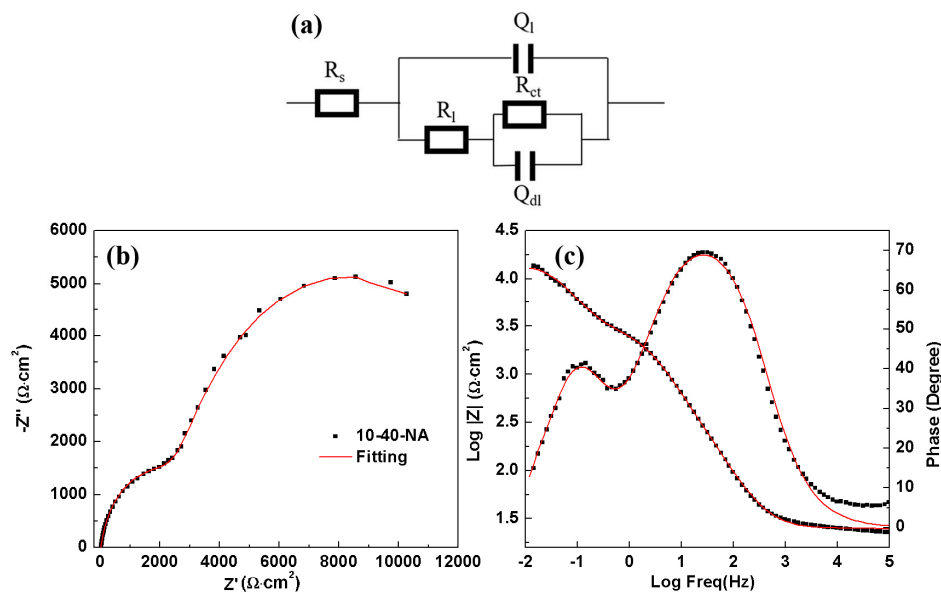
Figure 7. (**a**) Equivalent circuit of AA 2024 in 0.1 M NaCl solution; (**b**) Nyquist and (**c**) Bode example of the fitted result for a selected EIS diagram (10-40-NA).
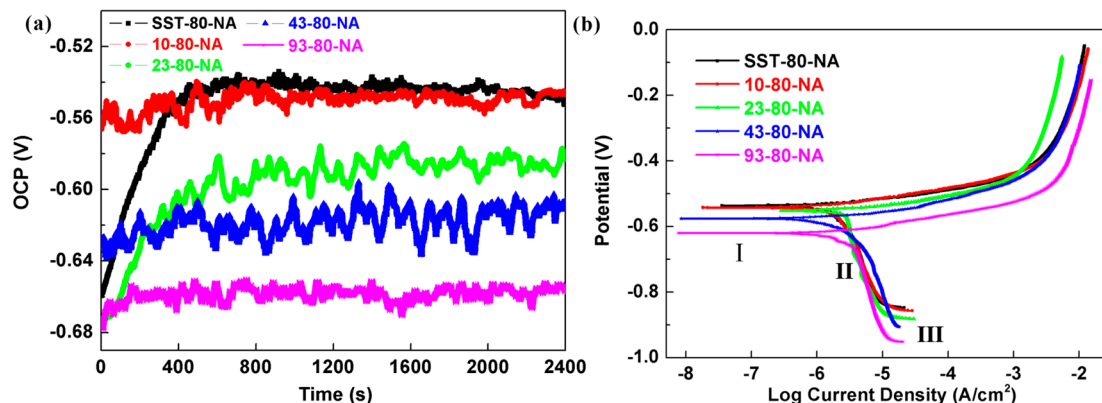
Table 4. The parameters of the EIS of samples with different strain in 0.1 M NaCl solution.

Sample ID	R_s ($\Omega \cdot cm^2$)	Y_1 ($10^{-5}\ \Omega^{-1} \cdot cm^{-2} \cdot s^n$)	n_1	R_1 ($\Omega \cdot cm^2$)	Y_{dl} ($10^{-4}\ \Omega^{-1} \cdot cm^{-2} \cdot s^n$)	n_{dl}	R_{ct} ($\Omega \cdot cm^2$)
10-27-NA	25.08	5.04	0.8	2601	3.117	0.88	5150
10-40-NA	24.88	4.131	0.871	3328	2.813	0.92	6209
10-50-NA	26.13	4.087	0.858	4475	2.656	0.91	6750
10-80-NA	24.34	3.895	0.871	4452	2.612	0.92	8939

Figure 8a describes the measurement of the OCP of the AA 2024 with different pre-aging time (80% strain) in 0.1 M NaCl solution. The results show that the OCP shifts to more negative potential direction with the increase of pre-aging time. The OCP of the 43-80-NA and 93-80-NA samples remained at a low level, whereas the SST-80-NA took about 460 s to reach a steady state. The OCP of SST-80-NA and 10-80-NA are around −0.55 V, which is higher than that of 23-80-NA (−0.59 V), 43-80-NA (−0.61 V) and 93-80-NA (−0.66 V), showing lower corrosion tendencies. Figure 8b shows

the PDP plots and three stages were also observed in the cathodic branch. The E_{corr} and (I_{corr}) are displayed in Table 5, and the E_{corr} of 93-80-NA is about 0.1 V lower than that of SST-80-NA (larger than the difference of 0.03 V between samples with different strains, Table 3). The E_{corr} of the other pre-aging time samples is located between these two samples (Table 5), indicating that the corrosion tendency increases with the prolongation of pre-aging time. The I_{corr} of samples are distributed between 1.23 to 1.82 μA/cm², indicating the faster corrosion rate increasing with pre-aging time. In the anodic branch, no passivation zone or obvious pitting potential was observed. The anodic current of all the samples increase rapidly and the anodic dissolution rate is large, which is associated with the microstructural features of the samples, especially the nature of the precipitates.


Figure 8. (**a**) The OCP and (**b**) PDP plots with scan rate of 1 mV/s of the natural aging AA 2024 with different pre-aging time in 0.1 M NaCl solution.

Table 5. The parameters of the PDP plots of samples with different pre-aging time in 0.1 M NaCl solution.

Sample ID	E_{corr} (V)	I_{corr} (μA/cm²)
SST-80-NA	-0.52 ± 0.01	1.23 ± 0.02
10-80-NA	-0.53 ± 0.01	1.38 ± 0.03
23-80-NA	-0.55 ± 0.01	1.46 ± 0.02
43-80-NA	-0.58 ± 0.02	1.48 ± 0.01
93-80-NA	-0.62 ± 0.02	1.82 ± 0.02

The EIS results of the samples in NaCl solution are displayed in Figure 9. Figure 9a shows two apparent semicircles in the Nyquist plot, indicating the response of two time constants. The arcs in low frequency in Nyquist plots varies greatly among samples, showing that there are great differences in pitting corrosion behavior of the samples with different pre-aging time due to the quite difference of precipitation characteristics as the STEM results show. Two time constants are observed in the Bode plots for the five samples (Figure 9b). The impedance values of the SST-80-NA and 10- 80-NA sample in middle and low frequencies are higher than those of the other three samples in the Bode plots, although such superiority is tiny. As shown in Table 6, the R_{ct} of the SST-80-NA (21,900 Ω·cm²) is one order of magnitude larger than that of the other samples. The R_{ct} decreased with the extension of the pre-aging time, and the R_{ct} of 93-80-NA is as low as 3031 Ω·cm², which is consistent with the data of I_{corr}. The Y_{dl} of the double layer capacitance increased with the pre-aging time, and this increasing trend, together with the declining trend of the R_{ct}, illustrates that the charge can easily transfer between Al alloy and solution. The Y_l and R_l were also changed irregularly for reasons discussed above.
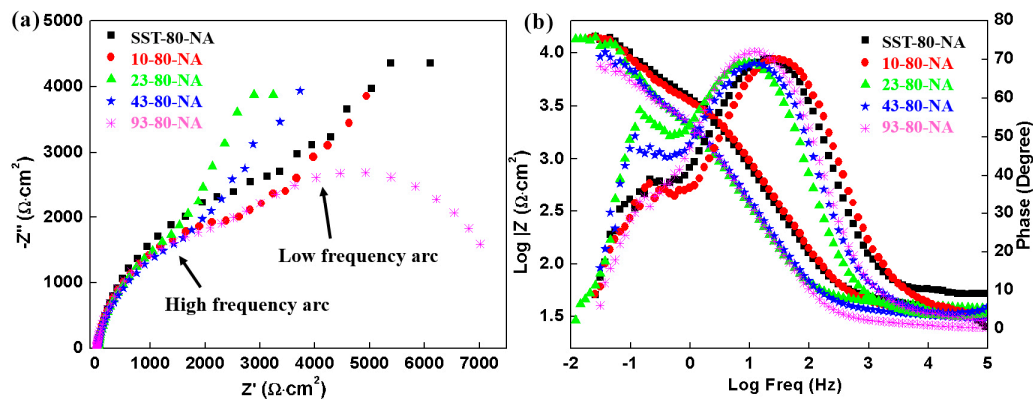
Figure 9. (**a**) Nyquist and (**b**) Bode plots of the AA 2024 with different pre-aging time in 0.1 M NaCl solution.

**Table 6.** The parameters of the EIS of samples with different pre-aging time in 0.1 M NaCl solution.

Sample ID	R_s ($\Omega \cdot cm^2$)	Y_1 ($10^{-5} \ \Omega^{-1} \cdot cm^{-2} \cdot s^n$)	n_1	R_1 ($\Omega \cdot cm^2$)	Y_{dl} ($10^{-4} \ \Omega^{-1} \cdot cm^{-2} \cdot s^n$)	n_{dl}	R_{ct} ($\Omega \cdot cm^2$)
SST-80-NA	28.69	3.398	0.8562	6046	1.949	0.96	21,900
10-80-NA	24.34	3.895	0.871	4452	2.612	0.92	8939
23-80-NA	27.99	6.919	0.8945	3702	2.718	0.91	8277
43-80-NA	23.09	6.543	0.8744	3829	2.906	0.94	6307
93-80-NA	26.57	6.331	0.9024	3647	3.423	0.89	3031

The AA 2024 with different pre-aging time were immersed in 0.1 M NaCl solution for 4 h and the corrosion morphologies are characterized by SEM as Figure 10a–d. The roughness of the samples decreased significantly compared with that before immersion and the preferential dissolution near the intermetallic particles is clearly visible. Pitting pits can be observed for SST-80-NA (Figure 10a), mainly around the second phase particles, but the matrix away from the second phase particles is basically not damaged. Table 7 is derived from the composition test results of Energy dispersion system (EDS) analysis in the graph. It can be explored that the composition of the matrix is basically the same as the receiving state alloy in Table 1, indicating the area affected by pitting is limited due to the relatively small volume fraction of fine GPB zones or clusters as shown in Figure 1a. The remnant is mainly rich in Cu, poor in Mg and Al, and about a few μm in size. It is believed that the remnant is mainly Al–Cu–Mg particles. In the early stage of immersion, the dealloying of Mg occurred, followed by the dealloying of Al [29]. In addition to the dissolution of Mg and Al and the enrichment of Cu, it is also noted that the substantial increase in O content, revealing that corrosion products (such as aluminum hydroxide and Al_2O_3) were accumulated in the remnant and its surroundings. Observations of these selective dissolutions are in agreement with local corrosion theory of the galvanic coupling between the precipitates and surrounding matrix [7].

In addition to the Al–Cu–Mg remnant particles and typical precipitate pitting morphology, a larger size remnant particle is also observed for 10-80-NA (about 20 μm in length, Figure 10b). According to the composition test of the matrix and the remnant in Table 8, it is obvious that the contents of Si, Mn, Cu and Fe in the remnant are much higher than that of the matrix, which is consistent with the previous elemental map in Figure 3e. Therefore, the large particle is confirmed to be T phase. T-phase particles, though corroded, do not significantly contribute to the dissolution of the surrounding matrix [30,31], so we will no longer pay too much attention to the T phase in subsequent discussions.

Figure 10c is the pitting morphology of the 23-80-NA with a string of consecutive pits which are located in the elongated dislocation walls formed during rolling. The constituents of the remnants are shown in Table 9. The Cu content of remnant particles is up to 45.28%, and Mg and Al are poor, which is resulted from the selective dissolution of Al–Cu–Mg particles. The surface of the bare 93-80-NA after

4 h of immersion was heavily corroded (Figure 10d), which is obviously different from that of other samples. Based on its composition (Table 10), it can be revealed that the O content of the substrate is higher than the rest of the samples, indicating that the matrix is more oxidized. The corrosion products have high contents of O and Cl, and contain cracks. A large amount of white nanoparticles are scattered uniformly around the second phase particles, which are derived from the decomposition process of the second phase particles [29]. The severe pitting corrosion observed also explains why the samples are hard to passivate as shown in electrochemical results.
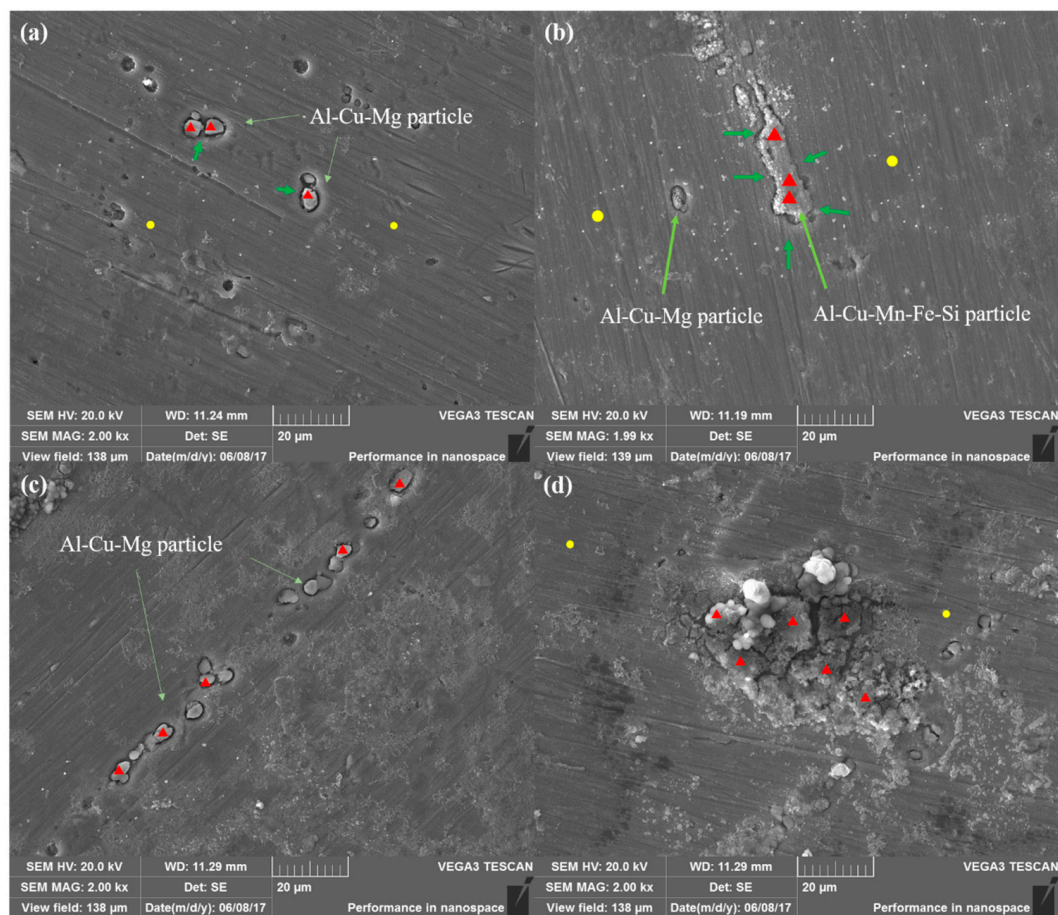
Figure 10. Surface topography of samples immersed in 0.1 M NaCl solution for 4 h: (**a**) SST-80-NA; (**b**) 10-80-NA; (**c**) 23-80-NA and (**d**) 93-80-NA. The red triangle is the test point of the chemical composition of the remnant. The green arrow is the test point of the chemical composition around the remnant and the yellow circle is the testing point of the matrix. The result of all the composition tests is the average of the test points.

Table 7. Chemical composition of the SST-80-NA sample.

Element	Matrix	Remnant	Remnant Periphery
O	1.35	23.65	30.55
Mg	1.47	0.78	1.08
Al	92.47	16.07	62.84
Si	0.14	0.08	0.20
Mn	0.48	0.49	0.51
Fe	0.00	0.23	0.12
Cl	0.06	2.33	0.61
Cu	4.04	56.38	4.11

Table 8. Chemical composition of the 10-80-NA sample.

Element	Matrix	Remnant	Remnant Periphery
O	1.69	14.32	20.24
Mg	1.49	0.34	1.09
Al	92.245	53.74	70.68
Si	0.08	3.87	0.32
Mn	0.435	8.33	1.24
Fe	0.06	11.41	1.27
Cl	0.04	0.1	0.10
Cu	3.96	7.89	5.07

Table 9. Chemical composition of the 23-80-NA sample.

Element	Remnant
O	25.77
Mg	1.00
Al	25.96
Si	0.14
Mn	0.17
Fe	0.21
Cl	1.48
Cu	45.28

Table 10. Chemical composition of the 93-80-NA sample.

Element	Matrix	Remnant
O	4.65	33.35
Mg	1.54	0.81
Al	89.72	48.42
Si	0.03	0.24
Mn	0.52	0.26
Fe	0.06	0.21
Cl	0.16	14.14
Cu	3.33	2.57

3.3. The Analysis of Passive Film

The main aspects of the corrosion process in NaCl solution is discussed above, and the previous electrochemical measurements and corrosion morphology results imply the microstructural features responsible for the performance differences of samples. Oxide films are easily formed on the Al alloy surface in the air, which would also be influenced by the microstructure [13,23,32]. However, no passivation behavior occurred in the NaCl solution as shown above, so we intended to apply the borate buffer solution to promote the formation of passive film. Electrochemical test results show that the corrosion behavior is greatly affected by the pre-aging time or the corresponding precipitation features, so we selected three typical samples with different pre-aging time (10 h, 43 h, 93 h) for the research of passivation behavior, as they have large differences in the corrosion behavior and precipitation characteristics.

Figure 11a depicts the evolution of the OCP of the samples with different pre-aging time. Within 1 h of testing, the OCP of all samples move toward the more noble values direction without potential transients as shown in Figure 4a or Figure 7a, indicating the formation of compact passive film. The stable OCP is about 0.2 V higher than that in NaCl solution. The borate buffer solution promoted the formation of passive films thus reduced the corrosion probability, which would be confirmed by the following anodic polarization curves and EIS. Representative anodic polarization tests after the OCP stabilization in borate buffer solution are shown in Figure 10b. As expected, the polarization

plots for the different pre-aging time samples are almost identical in shape and form, where the current varies linearly and steadily near the corrosion potential. This is consistent with the fact that the polarization response is largely depend on the composition of the sample and frequently is less sensitive to intermetallic or microstructure [33]. The passive zones of the three types of samples are basically sharing the same. Compared with their counterparts in NaCl solution (Table 5), the E_{corr} are increased by about 0.25 V and I_{corr} are two orders of magnitude higher (Table 11). It was observed that the value of I_{corr} increased with increasing the pre-aging time. It is clear that increasing the pre-aging time makes poor conditions for passive film formation with slightly lower protection behavior on 2024 Al alloy samples. Active-passive transform peaks and a basically constant current density in the passive zones are observed for all the three samples.
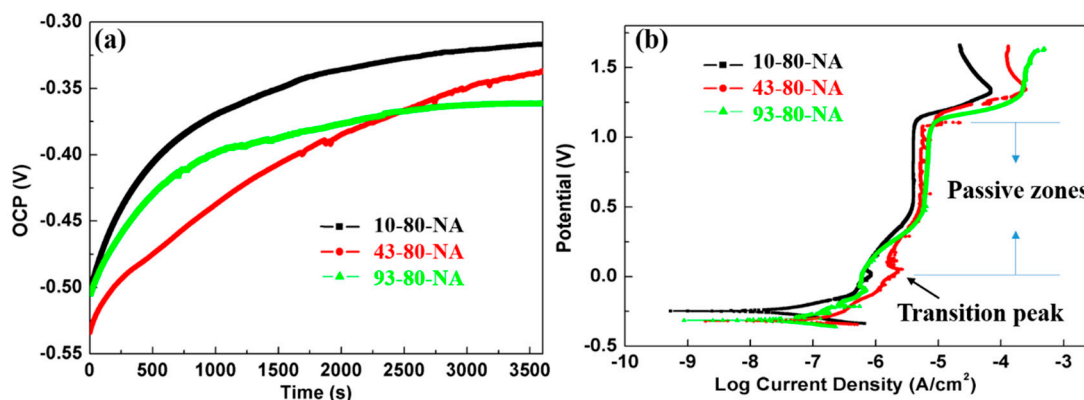
Figure 11. (**a**) The OCP and (**b**) Anodic polarization curves with scan rate of 1 mV/s of the AA 2024 with different pre-aging time in borate buffer solution.

Table 11. The parameters of the PDP plots of samples with different pre-aging time in 0.1 M NaCl solution.

Sample ID	E_{corr} (V)	I_{corr} (µA/cm^2)
10-80-NA	-0.25 ± 0.02	0.022 ± 0.003
43-80-NA	-0.32 ± 0.02	0.039 ± 0.004
93-80-NA	-0.32 ± 0.02	0.050 ± 0.003

Figure 12b illustrate the EIS results, which is a typical spectrum of passivation process with the electrochemical reaction process controlled by activation. Nyquist plots involve depressed semicircles with only one time constant, different from the EIS plots with two time constants for the samples in NaCl solution (Figures 5 and 8), as the typical low frequency/pitting corrosion time constant is absence. The Nyquist arc of the 10-80-NA sample is slightly larger than the other two samples, while the Bode diagram shows a smaller difference among them. Generally, the impedance modulus at low frequency (such as 0.1 Hz), can be regarded as a measure of corrosion resistance, and the modulus at 0.1 Hz in borate buffer solution (Figure 12) is one order of magnitude higher than that in NaCl solution (Figures 6 and 9), and the phase angle is also increased to close to 80°.

To characterize the property of the passive films, the equivalent circuit in Figure 13a with the elements of solution resistance (R_s), charge transfer resistance (R_{ct}) and constant phase element (Q_f) is applied. Q_f is related to the capacitance of the passive film. An example of fitting result (10-80-NA) is presented in Figure 12b,c showing a fine match. The parameters of the EIS results in borate buffer solution are given in Table 12. As shown in Table 12, the R_{ct} results reaching the order of magnitude to 10^5 $\Omega \cdot cm^2$, which is two orders of magnitude higher than the same sample in NaCl solution, revealing the stability of passive film and correlating with compactness or thickening of the passive film. The C_f was calculated from Equation (3) to be 6.93, 8.89 and 17.56 µF for 10-80-NA, 43-80-NA and 93-80-NA,

respectively. The capacitance of double layer in smooth electrode is approximately 60 μF/cm^2 [26], while the capacitance of the passive film in this work is varied between 8 and 18 μF/cm^2, and this is because the formation of passive film change the surface state including the exposure area, thickness and dielectric constant of the electrode. The passive film capacitive (*C*) is determined by Equation (4) [13]:

$$d = \varepsilon\varepsilon_0 A/C \tag{4}$$

where ε reveals the dielectric constant of the passive film (usually 10 for Al alloys), ε_0 represents the vacuum permittivity, *d* is the thickness of the passive film and *A* is the effective exposure area (0.49 cm^2). Usually, the change of the passive film capacitance is regarded as an indicator of the variation of its thickness (*d*). For the samples in Figure 11, *d* are 0.63, 0.49 and 0.25 nm, respectively (values calculated with Equation (4)). Therefore, the reciprocal passive film capacitance is proportional to the thickness, which decreases as pre-aging time increases. But generally speaking, according to the EIS spectra and the fitting results, it can be concluded that the passivation behavior of different samples is similar.
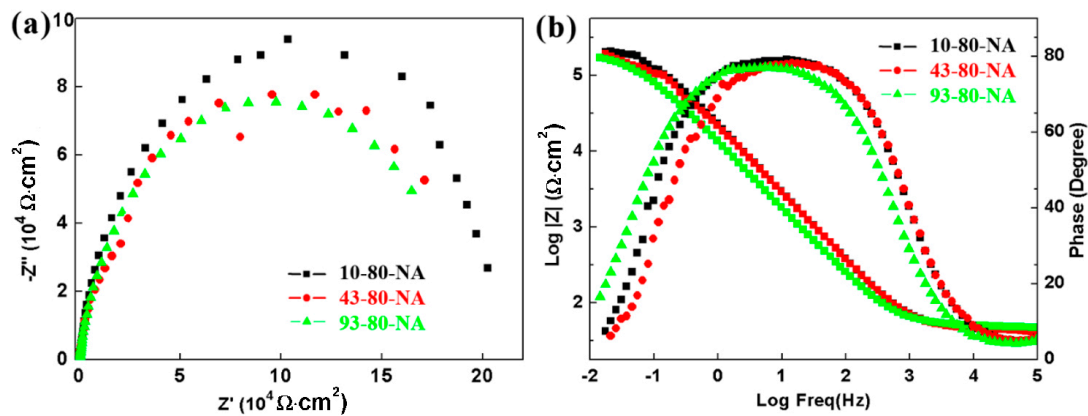
Figure 12. (**a**) Nyquist and (**b**) Bode plots of the AA 2024 with different pre-aging time in borate buffer solution.

Table 12. The parameters of the EIS of samples in borate buffer solution.

Sample ID	R_s (Ω·cm^2)	Y_r (10^{-6} Ω^{-1}·cm^{-2}·s^n)	n_r	R_{ct} (10^5 Ω·cm^2)
10-80-NA	46.32	8.282	0.88	2.207
43-80-NA	42.87	6.419	0.8869	2.021
93-80-NA	49.61	1.495	0.8719	1.883

According to the Mott–Schottky theory [34], the space charge capacitance of the *n*-type and *p*-type semiconductors can be expressed by Equations (5) and (6), respectively:

$$C^{-2} = C_H^{-2} + C_{SC}^{-2} = \frac{2}{\varepsilon\varepsilon_0 eA^2 N_D}\left(E - E_{fb} - \frac{KT}{e}\right) \tag{5}$$

$$C^{-2} = C_H^{-2} + C_{SC}^{-2} = -\frac{2}{\varepsilon\varepsilon_0 eA^2 N_A}\left(E - E_{fb} - \frac{KT}{e}\right) \tag{6}$$

where ε is dielectric constant of the passive film (usually 10 for passive film formed on Al alloy [34], the same as in Equation (4)), ε_0 is the vacuum Permittivity (8.854×10^{-12} F·m^{-1}), *e* is electron charge (1.602×10^{-19} C), A^2 is the geometric surface area of the film. N_D and N_A are the acceptor concentration of *n*-type semiconductor and donor concentration of *p*-type semiconductor, respectively. E_{fb} is the flat band potential. *E* is the applied potential, *K* is the Boltzmann constant (1.38×10^{-23} J/K), *T* is the absolute temperature. By measuring the capacitance of the space charge layer at different potentials

and the plot of $1/C^2$ vs. E, the slope of the plot can be used to determine the type of the semiconductor based on Formulas (5) and (6), and the concentration of the acceptor or donor could be obtained. The capacitance is calculated according to Equation (7):

$$C = (-Z_{im}2\pi f)^{-1} \tag{7}$$

where Z_{im} is the imaginary part of impedance, and f is the measurement frequency (1000 Hz for the present work).
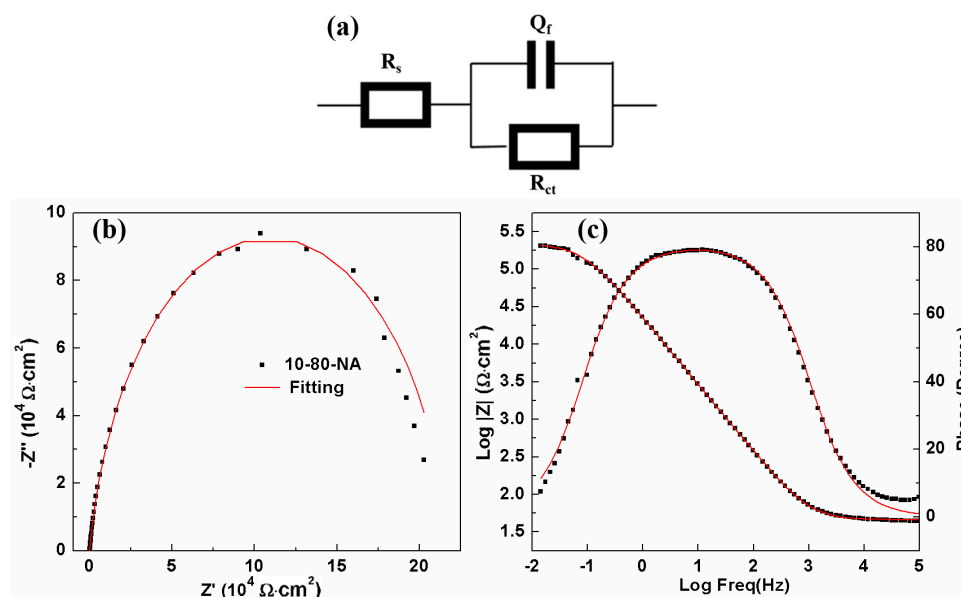

Figure 13. (**a**) Equivalent circuit of AA 2024 in borate buffer solution. (**b**) Nyquist and (**c**) Bode example of the fitted result for a selected EIS diagram (10-80-NA).

Figure 14a displays the Mott–Schottky plots of the AA 2024 in borate buffer solution, showing positive slope in the range of −0.1 V–0.1 V, which indicates *n*-type semiconductor features of the passive films. It is noteworthy that the voltage range is just in the passive region based on Figure 11b. *N*-type semiconductor behavior demonstrates that the primary defects in the passive film are oxygen vacancies. The donor concentration (N_D) of the passive film calculated from the slopes is displayed in Figure 14b. The sample with the shortest pre-aging time exhibits the minimum donor concentration, the lowest defect density and lower corrosion tendency. This phenomenon is in excellent agreement with the variation of the R_{ct} (Table 12), demonstrating that the passive film performance is slightly deteriorated by increasing the pre-aging time. According to point defect model [22], the passive film has a large number of point defects, such as oxygen vacancies (donors) and cations (donors). The motion of defects promotes the formation of the passive film. As a result, more oxygen vacancies can lead to loose passivation films and cation vacancies that may make metals more soluble. Nevertheless, the difference among the three samples is very small, all of which are the orders of magnitude 10^{20} cm^{-3}.

The passive film morphology of 43-80-NA sample immersed in borate buffer solution are exhibited in Figure 15 (basically the same for the rest samples, not shown here). The intermetallics remained intact under the passive film without visible corrosion after 4 h of immersion (Figure 15a) rather than suffering pitting as in the sodium chloride solution (Figure 10). The scratches left by sandpaper was gradually covered with the passive film in the first 4 h, and finally little trace of scratches was observed after 24 h. It is seen in the EDS maps that the passive film contains high amounts of O and some B, all of which are the characteristic elements in the borate buffer solution. Active element Mg was also detected, indicating that the substrate is effectively protected by the passive film. Denser and thicker passive films have been formed and some corrosion inhibitor crystals with high oxygen content

(Oxygen map is brighter in color) are attached to the surface after 24 h. Some "black holes" in the map are observed for the Al alloy substrate element (Al, Mg and Cu), but this is due to the coverage of the second phases by corrosion inhibitor crystals rather than the depletion of elements (Figure 15b′). The passive films fabricated by immersing in borate buffer solution exhibit excellent anticorrosive effect as the coating generated by steam [35] or microarc oxidation [27].
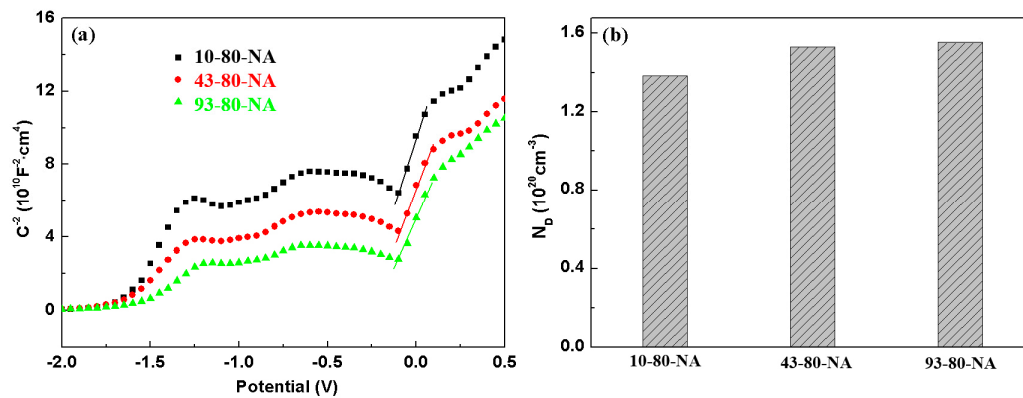
Figure 14. (**a**) Mott–Schottky plots and (**b**) the donor concentration in the passive film of the AA 2024 with different pre-aging time in borate buffer solution.
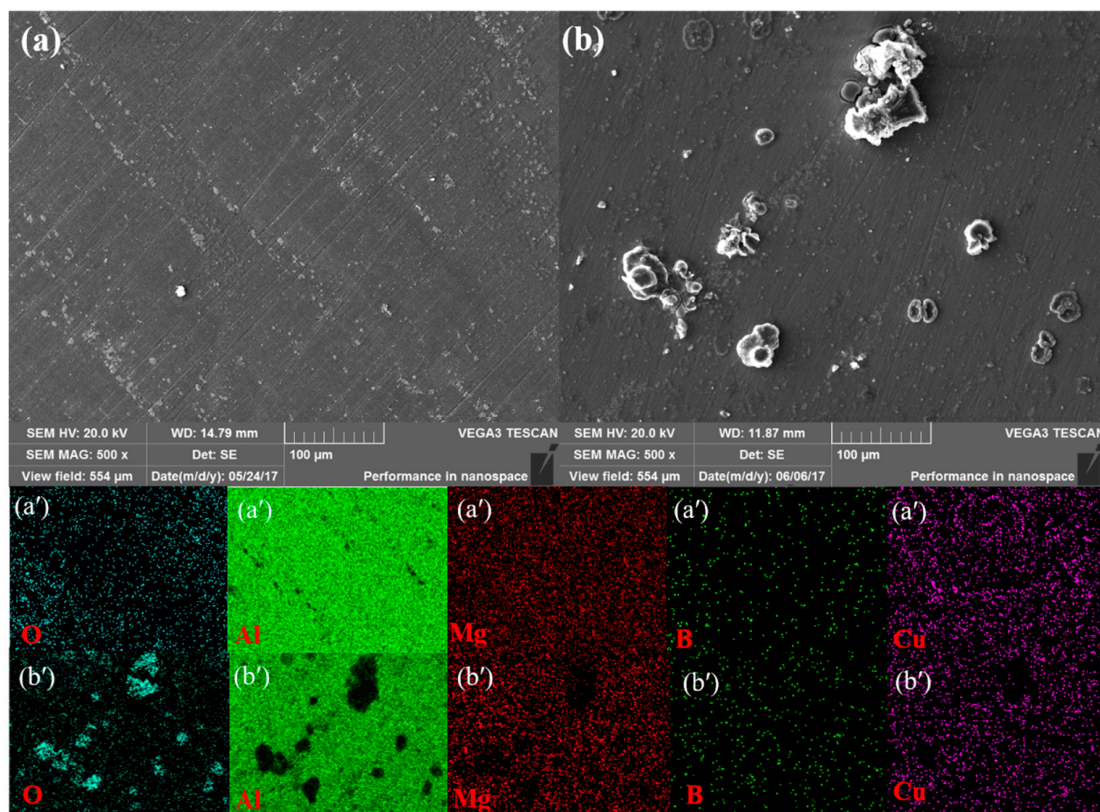
Figure 15. Surface morphology of passive films of 43-80-NA immersed in borate buffer solution for (**a**) 4 h and (**b**) 24 h. (**a′**) and (**b′**) are the EDS maps from (**a**) and (**b**), respectively.

4. Discussion

The corrosion resistance of samples with larger strain is a little better than that of small strain samples, as shown in Figures 5 and 6. While the deterioration of corrosion resistance is much more

significant with the increase of the pre-aging time, such as the negative shift of OCP and E_{corr} (Figure 8) and the significant decrease of R_{ct} (Table 6). The different influence of the two factors is attributed to the precipitate phase and will be discussed as follows.

4.1. Precipitation Evolution

Some atomic clusters or GPB zones were observed in the SST-80-NA sample (Figure 1a), which are believed to be generated in the NA process considering that it did not contain the pre-precipitates, especially after the rolling process [1]. With the increase of pre-aging time, both the volume fraction and the size of the precipitation phase increase. These precipitates (GPB/S′/S) would (partially) dissolve in the rolling process and the dissolution of these deformable precipitates is attributed to the release of the strain energy and the interfacial energy accumulated in the precipitate during rolling, as well as the release of the interfacial energy of the S′ phase/matrix [17].

Based on our previous research [1], the Cu and Mg atoms will be enriched on the dislocation line after rolling. This is due to the release of Cu and Mg atoms from the re-dissolved S′ phase and GPB zones and the diffusion to the matrix during deformation. The high density dislocations from deformation are the channels of rapid diffusion of solute atoms, thus the solute atoms tend to segregate along the dislocation structure. We call such structure enriched in solute atoms as "precipitate embryo" (Figure 16) [1]. The changes of microstructure may include when the Al alloy is aged after cold deformation: Dislocation recovery (annihilation), recrystallization (grain growth) and second phase precipitation. As the NA temperature was very low (room temperature), dislocation or grain size recovery are negligible. Therefore, in the NA process, the main occurrence was the nucleation and growth of the precipitate phase on the basis of embryo structures (Figure 16). The formation of GPB zone or S phase in NA can be understood from several aspects [11]: (i) In Al alloy, GP (GPB) zone is preferentially formed in NA process [36] due to a very low interfacial energy [37]; (ii) under NA conditions, the diffusivity of Cu is not high enough, which is beneficial to the formation of stable Cu–Mg clusters (or GPB zones), and conversely, the formation of S precipitates (Al_2CuMg); (iii) the dislocation density of the rolling sample is very high as shown in all the STEM pictures, and it is difficult to recover during the NA process. Therefore, the nucleation sites (dislocations/embryo) may be highly dense. This also facilitates the formation of nanoscale S phase (Al_2CuMg) precipitates through the short-range diffusion of Cu and Mg atoms at room temperature. The reasons why the re-aging precipitated phase is preferentially nucleated at the intragranular embryos rather than at the grain boundary are described in detail in the previous article [1].

In the rolling process, some large S phase particles cannot be re-dissolve due to the great hardness or the excessive number of precipitates. The final precipitation phase of these samples thus consists of two parts: Undissolved pre-precipitated phase (larger size) and NA precipitates (smaller size) from precipitate embryos.
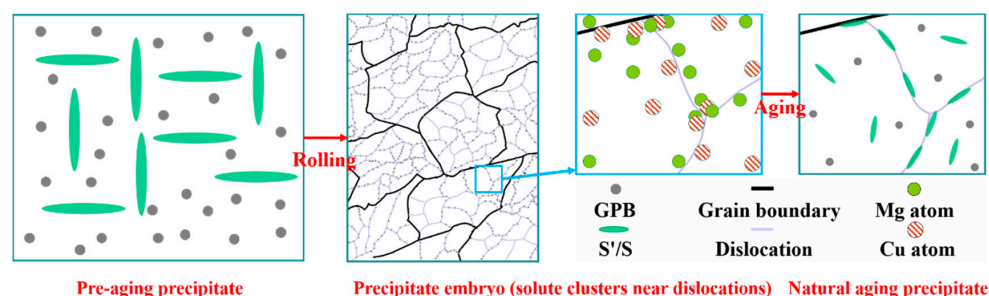

Figure 16. A schematic showing the precipitation evolution in AA 2024 [1].

4.2. Analysis of Corrosion Results

From the above corrosion morphologies and the EDS results, it can be revealed that the Mg and Al are the major corrosion-promotion elements for the studied AA 2024 during the electrochemical corrosion experiments. The anodic reactions are mainly the transformation of Mg and Al atoms on the surface of second phase particles. The second phase particles, such as GPB/S′/S phase, have stronger electrochemical activity relative to the matrix due to the presence of Mg. Mg and Al is gradually depleted by selective dissolution:

$$Al \rightarrow Al^{3+} + 3e \tag{8}$$

$$Mg \rightarrow Mg^{2+} + 2e \tag{9}$$

and the remnant is gradually changed from anodic properties to cathodic properties compared to the matrix resulting in the anodic dissolution of the surrounding matrix [29]. The corresponding cathodic reactions are mainly oxygen reduction or hydrogen evolution reactions. Since the microstructural characteristics of different samples are basically the same except for the aging precipitates as shown in Figures 1–3, the observed differences of samples in corrosion resistance can be mainly attributed to the precipitates present in the microstructure.

The electrochemical results of samples processed by different strain were decided by precipitate phase and grain size. The increase in strain induce the formation of fine GPB zones as shown in Figure 3b, due to the formation of precipitate embryos. While only large S precipitations were observed in samples with smaller strain (Figure 3a). According to some previous studies [31,38], it is found that there is a critical size in Al–Cu–Mg alloy below which the S phase is free of corrosion due to the coverage of the oxide film. Therefore, the corrosion resistance of the smaller strain samples, which mainly contains the undissolved large size S phase, is poor. In addition, the determination of grain size shows that it decreases with the increase of strain as illustrated in Section 3.1, which also contributes to superior corrosion resistance [23,24,32,39].

The corrosion resistance is decreased by increasing the pre-aging time, which can be attributed to the evolution of a small number of GPB zones (Figures 1a and 3b) to a large quantity of S phases (Figure 2) on the microstructure. The following changes happened during the whole two-stage aging and deformation, according to the STEM characterizations and our previous studies [1]. (i) As the pre-aging time increases, the number and size of precipitates increases, and the GPB zones gradually grow into the S phase; (ii) in the rolling process, the precipitate embryos are gradually generated at the expense of precipitate dissolution. The precipitates of the sample with short pre-aging time were almost completely dissolved (10 h, 23 h), while many undissolved S phase particles are retained in long pre-aging time samples (43 h, 93 h); (iii) in the NA process, fine GPB zones gradually nucleate and grow on the basis of the embryo. The number of embryo increases with the pre-aging time. The schematic diagram of the variation trend of the number of undissolved large pre-precipitates and fine NA precipitates from embryos is illustrated in Figure 17.

The corrosion resistance of SST-80-NA sample was the best in all samples because only a small amount of small-sized GPB zones or clusters at the early stage of nucleation were formed in in the NA process as shown in Figure 1a. It is unable to form an embryo since it is essentially free of precipitates prior to deformation and the solute atoms are nearly uniformly distributed throughout the entire coarse grain.
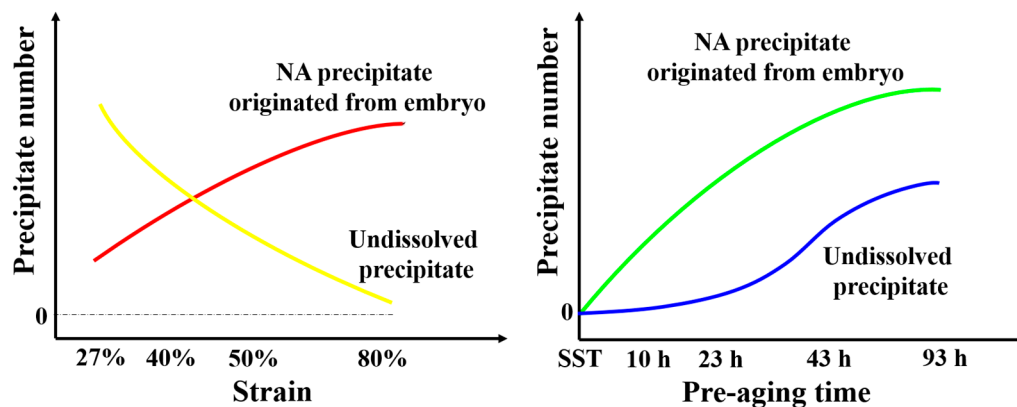
Figure 17. Schematic diagram of variation trend of precipitated phase number.

4.3. Factors Influencing Passive Film

The undissolved S phase and T phase in the rolling process, and the newly formed Al–Cu–Mg particles in the NA process have a significant influence on the subsequent corrosion process, but have less influence on the passivation process. The results obtained from the electrochemical tests and SEM morphologies revealed the formation of compact passive films with excellent blocking effect, due to the inhibition effect of the borate buffer solution (According to Pourbaix diagram [40,41]). The borate buffer solution can be adsorbed on the surface of the Al alloy as shown in Figure 15, reducing the contact between the electrode and the solution thus reducing the dissolution rate of the anode.

Yet the protection behavior is slightly deteriorated by increasing pre-aging time (Tables 11 and 12). The Mott–Schottky results reveal that the donor density, which is affected by internal defects distribution, increased with the pre-aging time. Generally, a large number of matrix/intermetallic interfaces are the priority sites of corrosion initiation [13]. Therefore, the large size S precipitations are always exposed sites, while the small size GPB zones are easily covered by the passive films. Thus, by increasing the pre-aging time, the passive film will become more defective for the undissolved large S precipitations and NA precipitates will increase simultaneously as discussed above.

This study takes AA 2024 as an example. However, the basic principles contained here are relatively common and thus might be applicable to other precipitation-containing systems as well. Potential opportunities exist to extend the combinations of mechanical and corrosion resistance exhibited by these materials by creating microstructures with heterogeneity and the critical size of precipitates are remain in the range where they are free of electrochemically activity. This work may be the first step in developing a new type of "stainless" Al alloys that has sufficient strength without the corrosion susceptibility limitations imposed on conventional Al–Cu–Mg alloys.

5. Conclusions

(1) With the increase of pre-aging time and the decrease of the rolling strain, the number of precipitated phase increases gradually and the size becomes larger.

(2) The corrosion resistance of the large strain samples is better because it mainly contains fine GPB zones from embryos with only a small amount of large size S phase, and the grain size is finer.

(3) The corrosion resistance of SST-80-NA was the best in all samples because only a small amount of small-sized GPB zones or clusters were formed inside. The corrosion resistance is deteriorated by increasing the pre-aging time, due to the simultaneous increase of undissolved large S precipitations and NA precipitates.

(4) The increase of the pre-aging time increased the favorable corrosion initial sites (matrix/intermetallic interfaces), leading to the decrease of the protective performance of the passive film.

Author Contributions: Tao Zhang searched literature, designed the study, collected experimental data, analyzed the experimental data and wrote the paper; Hongyun Luo designed the conception and edited the paper; Yuqin Su guided the experimental operation and data processing, designed some experiments and revised the paper; Pingwei Xu, Jun Luo and Sijie Li completed part of the experiments, analyzed part of the experimental data and revised the paper.

Conflicts of Interest: The authors declare no conflict of interest.

References

1. Xu, P.; Luo, H. Improving the ductility of nanostructured Al alloy using strongly textured nano-laminated structure combined with nano-precipitates. *Mater. Sci. Eng. A-Struct.* **2016**, *675*, 323–337. [CrossRef]

2. Xu, P.; Luo, H.; Li, S.; Lv, Y.; Tang, J.; Ma, Y. Enhancing the ductility in the age-hardened aluminum alloy using a gradient nanostructured structure. *Mater. Sci. Eng. A-Struct.* **2017**, *682*, 704–713. [CrossRef]

3. Ma, K.; Wen, H.; Hu, T.; Topping, T.D.; Isheim, D.; Seidman, D.N.; Lavernia, E.J.; Schoenung, J.M. Mechanical behavior and strengthening mechanisms in ultrafine grain precipitation-strengthened aluminum alloy. *Acta Mater.* **2014**, *62*, 141–155. [CrossRef]

4. Ma, K.; Hu, T.; Yang, H.; Topping, T.; Yousefiani, A.; Lavernia, E.J.; Schoenung, J.M. Coupling of dislocations and precipitates: Impact on the mechanical behavior of ultrafine grained Al-Zn-Mg alloys. *Acta Mater.* **2016**, *103*, 153–164. [CrossRef]

5. Zhu, D.Q.; van Ooij, W.J. Corrosion protection of AA 2024-T3 by bis-[3-(triethoxysilyl)propyl]tetrasulfide in sodium chloride solution. Part 2: Mechanism for corrosion protection. *Corros. Sci.* **2003**, *45*, 2177–2197. [CrossRef]

6. Boag, A.; Hughes, A.E.; Glenn, A.M.; Muster, T.H.; McCulloch, D. Corrosion of AA2024-T3 Part I. Localised corrosion of isolated IM particles. *Corros. Sci.* **2011**, *53*, 17–26. [CrossRef]

7. Moreto, J.A.; Marino, C.E.B.; Bose Filho, W.W.; Rocha, L.A.; Fernandes, J.C.S. SVET, SKP and EIS study of the corrosion behaviour of high strength Al and Al-Li alloys used in aircraft fabrication. *Corros. Sci.* **2014**, *84*, 30–41. [CrossRef]

8. Ralston, K.D.; Birbilis, N.; Cavanaugh, M.K.; Weyland, M.; Muddle, B.C.; Marceau, R.K.W. Role of nanostructure in pitting of Al-Cu-Mg alloys. *Electrochim. Acta* **2010**, *55*, 7834–7842. [CrossRef]

9. Guan, L.; Zhou, Y.; Zhang, B.; Wang, J.Q.; Han, E.H.; Ke, W. Influence of aging treatment on the pitting behavior associated with the dissolution of active nanoscale beta-phase precipitates for an Al-Mg alloy. *Corros. Sci.* **2016**, *103*, 255–267. [CrossRef]

10. Parel, T.S.; Wang, S.C.; Starink, M.J. Hardening of an Al-Cu-Mg alloy containing Types I and II S phase precipitates. *Mater. Des.* **2010**, *311*, S2–S5. [CrossRef]

11. Zhao, Y.L.; Yang, Z.Q.; Zhang, Z.; Su, G.Y.; Ma, X.L. Double-peak age strengthening of cold-worked 2024 aluminum alloy. *Acta Mater.* **2013**, *61*, 1624–1638. [CrossRef]

12. Wang, Z.; Chen, P.; Li, H.; Fang, B.; Song, R.; Zheng, Z. The intergranular corrosion susceptibility of 2024 Al alloy during re-ageing after solution treating and cold-rolling. *Corros. Sci.* **2017**, *114*, 156–168. [CrossRef]

13. Khatami, R.; Fattah-alhosseini, A.; Keshavarz, M.K. Effect of grain refinement on the passive and electrochemical behavior of 2024 Al alloy. *J. Alloys Compd.* **2017**, *708*, 316–322. [CrossRef]

14. Liu, G.; Zhang, G.J.; Jiang, F.; Ding, X.D.; Sun, Y.J.; Sun, J.; Ma, E. Nanostructured high-strength molybdenum alloys with unprecedented tensile ductility. *Nat. Mater.* **2013**, *12*, 344–350. [CrossRef] [PubMed]

15. Vidal, V.; Zhang, Z.R.; Verlinden, B. Precipitation hardening and grain refinement in an Al-4.2 wt % Mg-1.2 wt % Cu processed by ECAP. *J. Mater. Sci.* **2008**, *43*, 7418–7425. [CrossRef]

16. Huang, W.; Liu, Z.; Xia, L.; Xia, P.; Zeng, S. Severe plastic deformation-induced dissolution of θ'' particles in Al-Cu binary alloy and subsequent nature aging behavior. *Mater. Sci. Eng. A-Struct.* **2012**, *556*, 801–806. [CrossRef]

17. Huang, W.; Liu, Z.; Lin, M.; Zhou, X.; Zhao, L.; Ning, A.; Zeng, S. Reprecipitation behavior in Al-Cu binary alloy after severe plastic deformation-induced dissolution of θ' particles. *Mater. Sci. Eng. A-Struct.* **2012**, *546*, 26–33. [CrossRef]

18. Liu, Z.; Bai, S.; Zhou, X.; Gu, Y. On strain-induced dissolution of θ′ and theta particles in Al-Cu binary alloy during equal channel angular pressing. *Mater. Sci. Eng. A-Struct.* **2011**, *528*, 2217–2222. [CrossRef]

19. Murayama, M.; Horita, Z.; Hono, K. Microstructure of two-phase Al–1.7 at % Cu alloy deformed by equal-channel angular pressing. *Acta Mater.* **2001**, *49*, 21–29. [CrossRef]

20. Xu, P.; Luo, H.; Han, Z.; Zou, J. Tailoring a gradient nanostructured age-hardened aluminum alloy using high-gradient strain and strain rate. *Mater. Des.* **2015**, *85*, 240–247. [CrossRef]

21. Zou, J.; Luo, H.; Han, Z.; Lv, J. Investigation of texture characteristics of deformed layers in burnished 2024 aluminum alloy subsurface by EBSD. *Nanosci. Nanotechnol. Lett.* **2013**, *5*, 355–362. [CrossRef]

22. Lv, J.; Luo, H. Effect of surface burnishing on texture and corrosion behavior of 2024 aluminum alloy. *Surf. Coat. Technol.* **2013**, *235*, 513–520.

23. Lv, J.; Luo, H.; Xie, J. Experimental study of corrosion behavior for burnished aluminum alloy by EWF, EBSD, EIS and Raman spectra. *Appl. Surf. Sci.* **2013**, *273*, 192–198.

24. Lv, J.; Luo, H.; Liang, T. Investigation of microstructure and corrosion behavior of burnished aluminum alloy by TEM, EWF, XPS and EIS techniques. *Mater. Res. Bull.* **2016**, *83*, 148–154.

25. Lamaka, S.V.; Zheludkevich, M.L.; Yasakau, K.A.; Montemor, M.F.; Ferreira, M.G.S. High effective organic corrosion inhibitors for 2024 aluminium alloy. *Electrochim. Acta* **2007**, *52*, 7231–7247. [CrossRef]

26. Cheng, Y.L.; Zhang, Z.; Cao, F.H.; Li, J.F.; Zhang, J.Q.; Wang, J.M.; Cao, C.N. A study of the corrosion of aluminum alloy 2024-T3 under thin electrolyte layers. *Corros. Sci.* **2004**, *46*, 1649–1667. [CrossRef]

27. Wen, L.; Wang, Y.; Zhou, Y.; Ouyang, J.; Guo, L.; Jia, D. Corrosion evaluation of microarc oxidation coatings formed on 2024 aluminium alloy. *Corros. Sci.* **2010**, *52*, 2687–2696. [CrossRef]

28. Hsu, C.H.; Mansfeld, F. Technical note: Concerning the conversion of the constant phase element parameter Y-0 into a capacitance. *Corrosion* **2001**, *57*, 747–748. [CrossRef]

29. Zhu, D.Q.; van Ooij, W.J. Corrosion protection of AA 2024-T3 by bis-[3-(triethoxysilyl)propyl]tetrasulfide in neutral sodium chloride solution. Part 1: Corrosion of AA 2024-T3. *Corros. Sci.* **2003**, *45*, 2163–2175. [CrossRef]

30. Wang, J.; Zhang, B.; Zhou, Y.T.; Ma, X.L. Multiple twins of a decagonal approximant embedded in S-Al_2CuMg phase resulting in pitting initiation of a 2024Al alloy. *Acta Mater.* **2015**, *82*, 22–31. [CrossRef]

31. Wang, J.; Zhang, B.; Wu, B.; Ma, X.L. Size-dependent role of S phase in pitting initiation of 2024Al alloy. *Corros. Sci.* **2016**, *105*, 183–189. [CrossRef]

32. Lv, J.; Liang, T.; Wang, C.; Guo, T. The passive film characteristics of several plastic deformation 2099 Al-Li alloy. *J. Alloys Compd.* **2016**, *662*, 143–149.

33. Brunner, J.G.; Birbilis, N.; Ralston, K.D.; Virtanen, S. Impact of ultrafine-grained microstructure on the corrosion of aluminium alloy AA2024. *Corros. Sci.* **2012**, *57*, 209–214. [CrossRef]

34. Zhang, J.; Zhang, W.; Yan, C.; Du, K.; Wang, F. Corrosion behaviors of Zn/Al-Mn alloy composite coatings deposited on magnesium alloy AZ31B (Mg–Al–Zn). *Electrochim. Acta* **2009**, *55*, 560–571. [CrossRef]

35. Serizawa, A.; Oda, T.; Watanabe, K.; Mori, K.; Yokomizo, T.; Ishizaki, T. Formation of anticorrosive film for suppressing pitting corrosion on Al–Mg–Si alloy by steam coating. *Coatings* **2018**, *8*, 23. [CrossRef]

36. Sharma, V.M.J.; Kumar, K.S.; Rao, B.N.; Pathak, S.D. Effect of microstructure and strength on the fracture behavior of AA2219 alloy. *Mater. Sci. Eng. A-Struct.* **2009**, *502*, 45–53. [CrossRef]

37. Hamana, D.; Azizi, A. Low temperature post-precipitation after precipitation of β′ and β phases in Al-12 wt % Mg alloy. *Mater. Sci. Eng. A-Struct.* **2008**, *476*, 357–365. [CrossRef]

38. Ralston, K.D.; Birbilis, N.; Weyland, M.; Hutchinson, C.R. The effect of precipitate size on the yield strength-pitting corrosion correlation in Al–Cu–Mg alloys. *Acta Mater.* **2010**, *58*, 5941–5948. [CrossRef]

39. Ralston, K.D.; Birbilis, N.; Davies, C.H.J. Revealing the relationship between grain size and corrosion rate of metals. *Scr. Mater.* **2010**, *63*, 1201–1204. [CrossRef]

40. Fattah-Alhosseini, A.; Gashti, S.O. Corrosion behavior of ultra-fine grained 1050 aluminum alloy fabricated by ARB process in a buffer borate solution. *J. Mater. Eng. Perform.* **2015**, *24*, 3386–3393. [CrossRef]

41. Pourbaix, M. *Atlas of Electrochemical Equilibria in Aqueous Solutions*, 2nd ed.; NACE: Houston, TX, USA, 1974.